

A Low Mach Number Solver: Enhancing Stability and Applicability

Natalie Happenhofer ^{a,*,1}

Hannes Grimm-Strele ^{a,b,1}

Friedrich Kupka ^{a,2}

Bernhard Löw-Baselli ^a

Herbert Muthsam ^a

^a*University of Vienna, Faculty of Mathematics, Nordbergstraße 15, A-1090 Wien, Austria*

^b*Max-Planck Institute for Astrophysics, Karl-Schwarzschild-Strasse 1, 85741 Garching, Germany*

Abstract

In astrophysics and meteorology there exist numerous situations where flows exhibit small velocities compared to the sound speed. To overcome the stringent timestep restrictions posed by the predominantly used explicit methods for integration in time the Euler (or Navier–Stokes) equations are usually replaced by modified versions. In astrophysics this is nearly exclusively the anelastic approximation. Kwatra et al. [12] have proposed a method with favourable time-step properties integrating the *original* equations (and thus allowing, for example, also the treatment of shocks). We describe the extension of the method to the Navier-Stokes and two-component equations. – However, when applying this method to problems in convection and double diffusive convection (semiconvection) we ran into numerical difficulties. We describe our procedure for stabilizing the method. We also investigate the behaviour of Kwatra et al.’s method for very low Mach numbers (down to $Ma=0.001$) and point out its very favourable properties in this realm for situations where the explicit counterpart of this method returns absolutely unusable results.

Key words: hydrodynamics, Low Mach number, numerical method, stellar convection, double-diffusive convection

1991 MSC: 65M06, 65M08, 65M20, 65M60, 76F65

PACS: 97.10.Cv, 47.11.-j, 02.70.-c

1 Introduction

In astrophysics, meteorology and many other fields of physical and engineering sciences problems are studied which are characterized by vastly different timescales. In fluid flow the fast time scales are often set by diffusive processes, whereas the solution changes only on the much larger time scales set by the flow velocity or the sound speed. It is then general practice to make use of explicit time integration for the hyperbolic terms and to treat the diffusive terms implicitly. The latter task is facilitated by the fact that the resulting system of discretized equations is often linear and positive definite so that effective solution methods are available.

Frequently, however, the different scales originate from the macroscopic flow speed (small) and the sound speed (large). In addition, the sound waves may be known to be of little physical significance. Such a situation is ubiquitous in meteorology and geophysics (convection in the earth mantle). In stellar physics, these premises typically hold true for convection in the interior of the star, for example in the solar convection zone except for its outermost parts. Since an implicit time-advancement of the hyperbolic part is usually impractical due to, among others, a lack of efficient solvers for these terms, the usual solution strategy here is to eliminate the sound waves analytically and to discretize the modified equations only. A widely (in stellar physics: nearly exclusively) used way to accomplish that is to resort to the anelastic approximation [20] and its many variants or extensions. In meteorology, the use of so-called primitive equations is also widespread (cf.,[1],e.g.).

In [12] N.Kwatra et al. propose a semi-implicit method to solve Euler's equations numerically. From a physical point of view the advantage of this approach is that the method avoids any simplifications on the side of the basic equations themselves. As a consequence of that it is possible to treat physical phenomena for which the anelastic methods are neither designed nor appropriate, e.g. shocks. Indeed, in [12] a number of shock tube problems are satisfactorily treated as test cases. On the numerical side, the implicit part consists in the solution of an equation of a generalized Poisson equation only (equation (25)

* Corresponding Author

Email addresses: `natalie.happenhofer@univie.ac.at` (Natalie Happenhofer), `hannes.grimm-strele@univie.ac.at` (Hannes Grimm-Strele), `friedrich.kupka@univie.ac.at` (Friedrich Kupka), `bernhard.loew-baselli@univie.ac.at` (Bernhard Löw-Baselli), `herbert.muthsam@univie.ac.at` (Herbert Muthsam).

URLs: `http://www.mpa-garching.mpg.de/~fk/` (Friedrich Kupka), `http://www.univie.ac.at/acore/` (Herbert Muthsam).

¹ Supported by the Austrian Science Fund (FWF), project P20973

² Supported by the Austrian Science Fund (FWF), project P21742

in the present paper). For such equations, efficient solvers are relatively readily available. In [12], the method was developed in the framework of ENO type numerics.

These properties made the method an interesting candidate for inclusion in our ANTARES code [19] which is designed to cope with flows encountered in stellar physics ranging from low to high Mach numbers, including shocks. The original development in terms of ENO methodology complied well with the fact that ANTARES makes use of this methodology also in the other methods included for spatial discretization.

While after a few adaptations the Kwatra method performed well in the usual shock tube tests we performed, difficulties arose when applying it to the problem of semiconvection in stellar physics (double-diffusive convection; thermohaline convection in oceanography) in the same way we had, earlier on, successfully tackled similar problems with standard ENO methods. In semiconvection possibly slow (in terms of sound speed) convective motions take place. Already they enforce the calculations to span a large time interval in order to arrive at a relaxed, statistically steady state. In addition, between zones of ordinary convection thin, more or less horizontal sheets are situated where the transport of helium in the star (salt in the ocean) is provided by diffusive processes only which may easily make for even longer time scales [28]. Experience thus showed that the successful mastering of the shock tube problems as usually applied for validating numerical discretizations does not guarantee stability for long periods of time. Indeed, severe instabilities appeared in the course of time which rendered the calculations useless. It was therefore warranted to modify the original method so as to achieve stability even for long-term integrations.

The plan of the paper is the following. We first give a short description of the basics of Kwatra et al.'s method. Subsequently, we derive a pressure evolution equation which, unlike the original equation, takes also dissipative terms into account (radiative transfer in the diffusion approximation as adequate for stellar interiors). We also consider the case of two-component flows (semi- or thermohaline convection). We then describe the difficulties which resulted when applying this method to the semiconvection problem. Next we turn to the enhancement of stability which solved the numerical problems and discuss a few simulations.

Subsequently we describe the performance of Kwatra et al.'s method when dealing with very low Mach number flows (down to $\text{Ma}=0.001$). Here, Kwatra's method shows very satisfying behaviour which contrasts grossly with the completely useless results of the standard explicit method.

2 Numerical method

We model fluid flow by the set of compressible Navier-Stokes equations (NSE). A detailed derivation is found in [8] and [13]. For better legibility, all derivations are presented in one spatial dimension. The generalization to higher dimensions is easily done.

The compressible Navier-Stokes equations for a chemically homogeneous flow read

$$\begin{pmatrix} \rho \\ \rho u \\ e \end{pmatrix}_t + \begin{pmatrix} \rho u \\ \rho u \cdot u + P - \tau \\ eu + P \cdot u - u \cdot \tau - F_{\text{rad}} \end{pmatrix}_x = \begin{pmatrix} 0 \\ \rho g \\ \rho g u \end{pmatrix} \quad (1)$$

The state variables in the Navier-Stokes equations depend in principle on the spatial variable x and time t . The explicit dependencies are stated in Table 1. In general, the radiative source term $Q_{\text{rad}} = \nabla \cdot F_{\text{rad}}$ is determined as the stationary limit of the radiative transfer equation (see [16] for discussion and further references). However, we will only consider settings taking place in stellar regions which are optically thick, so this quantity can accurately be obtained by means of the diffusion approximation for radiative transfer, $Q_{\text{rad}} = \nabla \cdot F_{\text{rad}} = -\nabla \cdot (K \nabla T)$.

We now introduce our modified version of the semi-implicit numerical method of N.Kwatra et al [12]. To this end, we split the flux term in an advective part, a non-advective part and a viscous part,

$$F_{\text{ad}}(U) = \begin{pmatrix} \rho u \\ \rho u^2 \\ eu \end{pmatrix}, F_{\text{nonad}}(U) = \begin{pmatrix} 0 \\ P \\ P \cdot u \end{pmatrix}, F_{\text{vis}}(U) = - \begin{pmatrix} 0 \\ \tau \\ u \cdot \tau + K \nabla T \end{pmatrix}$$

The advective flux F_{ad} is calculated using the weighted essentially non-oscillatory (WENO) method proposed in [9]. This approach takes the computational val-

ues provided as cell averages $U_i = \frac{1}{h} \int_{x_{i-\frac{1}{2}}}^{x_{i+\frac{1}{2}}} v(\zeta) d\zeta$ and reconstructs the values

of $v(\zeta)$ at the cell interfaces by the means of an upwind biased interpolation operator. To ensure that every conservative variable is upwinded according to its characteristic speed, which is given by the corresponding eigenvalue of

$\rho = \rho(x, t)$	gas density
$u = u(x, t)$	flow velocity
ρu	momentum density
$P = P(x, t)$	gas pressure
$c = c(x, t)$	concentration of second species
g	gravitational acceleration
τ	viscous stress tensor for zero bulk viscosity
η	dynamic viscosity, appears in the definition of τ
$T = T(x, t)$	temperature
$K = K(\rho, T, c)$	radiative conductivity
$\kappa_T = K/(c_P \rho) = \kappa(T, \rho)$	radiative diffusivity
$e = e(x, t) = e_{\text{int}}(x, t) + e_{\text{kin}}(x, t)$	total energy density, sum of internal and kinetic energy densities
γ	adiabatic index ($\gamma = 5/3$) for ideal gas
$\kappa_c = \kappa_c(\rho, T, c)$	diffusion coefficient for species c

Table 1

Variables and parameters appearing in the model equations

the Jacobian DF_{ad} , the upwinding is done in the eigensystem where the equations decouple. However, due to the flux splitting approach the Jacobian of the advective flux F_{ad} reads

$$DF_{\text{ad}}(U) = \begin{pmatrix} 0 & 1 & 0 \\ -u^2 & 2u & 0 \\ -\frac{eu}{\rho} & \frac{e}{\rho} & u \end{pmatrix} \quad (2)$$

Since all eigenvalues of DF_{ad} are equal to u , we make use of the characteristic projection method [2] and apply componentwise upwinding to $F_{\text{ad}}(U)$.

The viscous part $F_{\text{vis}}(U)$ is calculated using a fourth order finite difference scheme presented in section 4.

2.0.1 The Algorithm

Firstly, we update the advective and the viscous part and add the vector of body forces to obtain an intermediate value of the conservative variables ρ^* , $(\rho u)^*$ and e^* . Since the pressure does not affect the density ρ we have

$$\rho^* = \rho^{(n+1)}.$$

As outlined in [12], the non-advection momentum and energy updates are

$$\frac{(\rho u)^{n+1} - (\rho u)^*}{\Delta t} = -\nabla P \quad (3)$$

$$\frac{e^{n+1} - e^*}{\Delta t} = -\nabla \cdot (Pu) \quad (4)$$

Dividing Eq. (3) by ρ^{n+1} and taking its divergence we obtain

$$\nabla \cdot u^{n+1} = \nabla \cdot u^* - \Delta t \nabla \cdot \left(\frac{\nabla P}{\rho^{n+1}} \right) \quad (5)$$

Similar to [12], we use the pressure evolution equation for the Navier-Stokes equations derived below in Section 2.1,

$$\frac{\partial P}{\partial t} + u \cdot \nabla P = -(\nabla \cdot u) \rho c_s^2 - \frac{2}{3\rho} (u \cdot \nabla \tau - \nabla \cdot (u \cdot \tau) + \nabla \cdot (K \nabla T)) \quad (6)$$

We take $\nabla \cdot u$ to be at time $n + 1$ through the timestep and substitute into (5) to obtain

$$\frac{\partial P}{\partial t} + u \cdot \nabla P = -\rho c_s^2 \nabla \cdot u^* + \rho c_s^2 \nabla \cdot \left(\frac{\nabla P}{\rho} \right) - \frac{2}{3\rho} (u \cdot \nabla \tau - \nabla \cdot (u \cdot \tau) + \nabla \cdot (K \nabla T)) \quad (7)$$

This is an advection-diffusion equation with a source term. We discretize the advective term and the source term using an explicit Euler-forward timestep and define the diffusive pressure implicitly at time $n + 1$. Apart from u^* , the velocity is taken at the old timestep, u^n . This leads to a general elliptic equation

$$\tilde{c} P^{n+1} - \nabla \cdot (\kappa \nabla P^{n+1}) = f \quad (8)$$

where

$$\tilde{c} = \frac{1}{\Delta t^2 \rho^n c_s^2} \quad (9)$$

$$\kappa = \frac{1}{\rho^{n+1}} \quad (10)$$

$$f = \frac{P^n - \Delta t u^n \cdot \nabla P^n}{\Delta t^2 \rho^n (c_s^n)^2} - \frac{1}{\Delta t} (\nabla \cdot u^*) - \frac{2}{3 \Delta t (\rho^n)^2 (c_s^n)^2} (u^n \cdot \nabla \cdot \tau^n - \nabla \cdot (u^n \cdot \tau^n) + \nabla \cdot (K \nabla T^n)) \quad (11)$$

As it is common in projection-like methods, we prescribe von Neumann boundary conditions,

$$\frac{\partial P^{n+1}}{\partial \vec{n}} \big|_{\partial \Omega} = 0 \quad (12)$$

\vec{n} denotes the outward pointing unit normal.

Taking over the formalism of the dual cell of [12] we interpolate the pressure to the cell interfaces via

$$P_{i+\frac{1}{2}} = \frac{P_{i+1} \rho_i + P_i \rho_{i+1}}{\rho_i + \rho_{i+1}} \quad (13)$$

and update equations (3) and (4) using a central difference quotient.

2.1 The Pressure Evolution Equation

Basically, the derivation of the pressure evolution equation follows the lines of [3], but instead of the Euler equations, we use the NSE. Although we start out using a general equation of state (EOS), the final shape of the pressure evolution equation depends on the equation of state considered, which is in our case the equation of state for ideal gas. However, a corresponding pressure evolution equation may be derived for any EOS.

We consider the general equation of state $P = P(\rho, \varepsilon)$ where $\varepsilon = e_{\text{int}}/\rho$. Taking the total derivative we have

$$\frac{DP}{Dt} = \left(\frac{\partial P}{\partial \rho} \right)_\varepsilon \frac{D\rho}{Dt} + \left(\frac{\partial P}{\partial \varepsilon} \right)_\rho \frac{D\varepsilon}{Dt} \quad (14)$$

Analysis of the Navier-Stokes Equations shows that

$$\frac{D\rho}{Dt} = -\rho \nabla \cdot u \quad (15)$$

$$\frac{D\varepsilon}{Dt} = \frac{-u \cdot (\nabla \cdot \tau) - P(\nabla \cdot u) + \nabla \cdot (u \cdot \tau) - \nabla \cdot (K \nabla T)}{\rho} \quad (16)$$

Using this and the general definition of the sound speed, $c_s^2 = \left(\frac{\partial P}{\partial \rho}\right)_\varepsilon + \frac{P}{\rho^2} \left(\frac{\partial P}{\partial \varepsilon}\right)_\rho$, we arrive at

$$\frac{\partial P}{\partial t} + u \cdot \nabla P = -(\nabla \cdot u) \rho c_s^2 - \left(\frac{\partial P}{\partial \varepsilon}\right)_\rho \frac{1}{\rho^2} (u \cdot \nabla \tau - \nabla \cdot (u \cdot \tau) + \nabla \cdot (K \nabla T)) \quad (17)$$

The partial derivative $\left(\frac{\partial P}{\partial \varepsilon}\right)_\rho$ is calculated using the equation of state. In case of ideal gas the EOS relating the pressure P to the internal energy ε reads

$$P = \frac{2}{3} \varepsilon \rho, \text{ naturally we have } \left(\frac{\partial P}{\partial \varepsilon}\right)_\rho = \frac{2}{3} \rho$$

Thus we arrive at equation (6).

2.2 Extension to a two-component flow

To model the behaviour of a two component fluid we add a concentration equation to the Navier-Stokes equations:

$$(\rho c)_t + (\rho c u)_x = (\rho \kappa_c \nabla c)_x \quad (18)$$

Splitting the fluxes as before leads to

$$F_{\text{ad2}}(U) = \begin{pmatrix} \rho u \\ \rho c u \\ \rho u^2 \\ e u \end{pmatrix}, F_{\text{nonad2}}(U) = \begin{pmatrix} 0 \\ 0 \\ P \\ P \cdot u \end{pmatrix}, F_{\text{vis2}}(U) = - \begin{pmatrix} 0 \\ \rho \kappa_c \nabla c \\ \tau \\ u \cdot \tau + K \nabla T \end{pmatrix}$$

and since all the eigenvalues of

$$DF_{\text{ad2}}(U) = \begin{pmatrix} 0 & 0 & 1 & 0 \\ -cu & u & c & 0 \\ -u^2 & 0 & 2u & 0 \\ -\frac{eu}{\rho} & 0 & \frac{e}{\rho} & u \end{pmatrix} \quad (19)$$

equal u , we apply componentwise upwinding to $F_{\text{ad2}}(U)$ and evaluate F_{vis2} as outlined for the one-component case.

Similar to the continuity equation, equation (18) is unaffected by the pressure, so $(\rho c)^* = (\rho c)^{n+1}$.

Basically, the momentum and energy updates (3),(4) are carried out as before, but since the pressure depends on the mass fraction c , the pressure evolution equation (6) takes a slightly different appearance.

Since $P = P(\rho, \varepsilon, c)$, equation (14) reads

$$\frac{DP}{Dt} = \left(\frac{\partial P}{\partial \rho} \right)_{\varepsilon, c} \frac{D\rho}{Dt} + \left(\frac{\partial P}{\partial \varepsilon} \right)_{\rho, c} \frac{D\varepsilon}{Dt} + \left(\frac{\partial P}{\partial c} \right)_{\rho, \varepsilon} \frac{Dc}{Dt} \quad (20)$$

Analysis of equation (18) shows that

$$\frac{Dc}{Dt} = \frac{\nabla \cdot (\rho \kappa_c \nabla c)}{\rho} \quad (21)$$

We use the equation of state for a perfect gas

$$P = \frac{R_{\text{gas}} \rho T}{\mu} \quad (22)$$

where μ denotes the mean molecular weight of our compound. It is related to the mass fraction c by $\mu = \frac{1}{c(1/atm_1) + (1-c)(1/atm_2)} \cdot atm_1$ and atm_1 and atm_2 refer to the atomic weight of the constituents of the fluid. In our case, we usually model a mixture of hydrogen and helium. c denotes the mass fraction of helium. Therefore, we have $atm_1 = 4$ being the atomic weight of helium whereas $atm_2 = 1$ is the atomic weight of hydrogen in non-ionized state. It is straightforward to include electron pressure in the EOS for partially or fully ionized gas. Thus, we arrive at

$$\left(\frac{\partial P}{\partial c}\right)_{\rho,\varepsilon} = -\frac{3}{4}R_{\text{gas}}\rho T \quad (23)$$

Whence the pressure evolution equation (6) reads

$$\frac{\partial P}{\partial t} + u \cdot \nabla P = -(\nabla \cdot u)\rho c_s^2 - \frac{2}{3\rho}(u \cdot \nabla \tau - \nabla \cdot (u \cdot \tau) + \nabla \cdot (K \nabla T)) - \frac{3}{4}R_{\text{gas}}T \nabla \cdot (\rho \kappa_c \nabla c) \quad (24)$$

and naturally, equation (11) becomes

$$\begin{aligned} f = & \frac{P^n - \Delta t u^n \cdot \nabla P^n}{\Delta t^2 \rho^n (c_s^n)^2} \\ & - \frac{1}{\Delta t}(\nabla \cdot u^*) - \frac{2}{3\Delta t(\rho^n)^2(c_s^n)^2}(u^n \cdot \nabla \cdot \tau^n - \nabla \cdot (u^n \cdot \tau^n) + \nabla \cdot (K \nabla T^n)) \\ & - \frac{3}{4\rho^n \Delta t (c_s^n)^2}R_{\text{gas}}T^n \nabla \cdot (\rho^n \kappa_c \nabla c^n) \end{aligned}$$

2.3 A Solver for the Generalized Poisson Equation

The fractional step method presented above relies on the prediction of the pressure at the next time step. This prediction is obtained by evaluating a Helmholtz type equation,

$$-\nabla(\kappa(x)\nabla\Phi(x)) + \tilde{c}(x)\Phi(x) = f(x) \quad (25)$$

It is crucial for the performance of the overall method to have an efficient numerical solver for equations of this type at hand. To fit into the existing ANTARES framework this solver is required to run in parallel and scale efficiently.

From an analytical point of view existence and uniqueness of a solution to equation (25) is guaranteed, if the coefficient functions $\kappa(x)$ and $\tilde{c}(x)$ are strictly positive over the entire domain. A quick check on (9) and (10) shows that these requirements are always met.

Various techniques are available to discretize equation (25). The discretization process transforms the partial differential equation into a system of linear equations. The solution of the linear system is the numerical approximation to the analytical solution of (25).

For discretization we preferred a finite element ansatz over a finite difference scheme, since the finite element technique leads to a symmetric and positive definite system matrix. A solution of the resulting linear system is determined by means of the preconditioned Conjugate Gradient Algorithm. As a preconditioner we use the incomplete Cholesky decomposition with fill-in. A detailed description of the methods is found in [5].

To test the scaling capability of our solver we solve the two-dimensional generalized Poisson equation (25) with $\kappa(x)$, $\tilde{c}(x)$, $f(x)$ as specified in (9) – (11) on a rectangular domain discretized with 800×800 grid points and employ a varying number of computational cores. The results are given in Table 2.

We point out that the run on a single core is algorithmically different, since in this case the generalized Poisson equation is solved using (only) the Conjugate Gradient algorithm. The Schur complement algorithm is first required solving the generalized Poisson equation on two cores and induces considerable overhead. The wall-clock times indicate that this overhead slows down the calculation by a factor of 12, i.e. employing the Schur complement method and solving the generalized Poisson equation on 12 cores takes as long as solving it on a single core employing just the Conjugate Gradient algorithm. Therefore, in our test the first real speedup is achieved employing 16 cores. However, the results also show that the wall-clock time decreases linearly beyond that. Hence, except for a constant factor, the Schur complement method scales optimally.

# cores	time in s	# cores	time in s
1	1.000	64	0.168
2	6.033	128	0.096
4	3.109	256	0.043
8	1.361	512	0.021
16	0.695	1024	0.016
32	0.345		

Table 2

Poisson solver scaling test: calculated at the IBM Power6 575 System at RZG.

2.4 Time Stepping

For time integration, the ANTARES framework provides the second and third order TVD Runge-Kutta schemes of [4]. N. Kwatra et al. suggested in [12] two variations of the temporal integration with Runge-Kutta methods. The first is to perform Runge-Kutta on just $F_{\text{ad}}(U)$ and $F_{\text{vis}}(U)$ with one final implicit

integration of $F_{\text{nonad}}(U)$. The second variation they suggest is to integrate $F_{\text{ad}}(U)$, $F_{\text{vis}}(U)$ and $F_{\text{nonad}}(U)$ for each Runge-Kutta stage. In [12] a better performance is reported employing the second variation. Since this coincides with our observations, we use the second variation in all our simulations.

In [12] a Courant-Friedrich-Levy condition based on an estimate of the maximum value of $|u|$ and the pressure gradient ∇p throughout the next timestep is derived,

$$\Delta t \left(\frac{|u|_{\text{max}} + \Delta t \frac{|p_x|}{\rho}}{\Delta x} \right) \leq 1 \quad (26)$$

However, the term corresponding to the pressure gradient can be neglected in the limit where $\Delta x \rightarrow 0$, since its contributions are of lower order (see [23] for a discussion of the treatment of lower order terms in stability analysis). Thus, we arrive at a timestep restriction exclusively due to the velocity of the flow,

$$\tau_{\text{fluid}} = c_{\text{adv}} \frac{\Delta x}{|u|_{\text{max}}} \quad (27)$$

Further restrictions on the timestep Δt are imposed by heat diffusion τ_{T} and the viscosity τ_{visc} . In case of a two component flow, the diffusion of the second component also leads to a time-step restriction, τ_{c} .

We define our timestep as

$$\Delta t = \min \{ \tau_{\text{T}}, \tau_{\text{visc}}, \tau_{\text{fluid}}, \tau_{\text{c}} \} \quad (28)$$

where

$$\tau_{\text{c}} = c_{\text{diff}} \cdot \frac{\Delta x^2}{\kappa_{\text{c}}} \quad \tau_{\text{T}} = c_{\text{diff}} \cdot \frac{\Delta x^2}{\kappa_{\text{T}}} \quad \tau_{\text{visc}} = c_{\text{diff}} \cdot \frac{\Delta x^2}{\nu}$$

c_{diff} and c_{adv} denote Courant numbers not necessarily equal.

The maximum Courant numbers $c_{\text{adv max}}$ and $c_{\text{diff max}}$ may be determined by (linear) von Neumann stability analysis (see, for example [23]). However, in case of $c_{\text{adv max}}$, the nonlinear WENO scheme must be linearized and the maximum Courant number obtained by linear stability analysis provides just an estimate. In fact, the maximum Courant number of WENO5 combined with the third order TVD Runge-Kutta method is predicted to be 1.43 but simple tests indicate that this solver becomes unstable at $c_{\text{adv}} = 1.0$ (see [25] and

[17]). Thus in practice we make sure to choose a Courant number smaller than the one theoretically possible.

The source term on the right hand side of equation (1), which represents buoyancy forces acting on the flow, also poses a restriction on the timestep but similarly to the restriction caused by the pressure gradient above its contributions are of lower order and hence only provide an accuracy but not a stability restriction.

3 Simulations in the Astrophysical Regime

3.1 Physical Setting

To set up a model of stellar convection, we follow the ansatz of [18] and [27] by considering a hydrostatically layered fluid column which is unstable against convection. In terms of the Schwarzschild criterion of convective instability [26] with x pointing along the direction of gravity, this reads

$$\frac{\partial T}{\partial x} > \left(\frac{\partial T}{\partial x} \right)_{\text{ad}} \quad (29)$$

From the outset we assume the gas to be ideal gas with a γ -law where $\gamma = 5/3$. The volume expansion coefficient is given by $\alpha = 1/(\gamma - 1)$ and the specific heat at constant pressure is $c_P = R_{\text{gas}}(1 + \alpha)$.

These data suffice to determine the adiabatic temperature gradient

$$\left(\frac{\partial T}{\partial x} \right)_{\text{ad}} = \frac{g}{c_P} \quad (30)$$

once we have specified the downward pointing constant gravity g .

We fix the temperature at the top and define a function $b(x)$ to be the ratio of the actual temperature gradient to the adiabatic one:

$$\frac{\partial T}{\partial x} = b(x) \left(\frac{\partial T}{\partial x} \right)_{\text{ad}} \quad (31)$$

We set $b(x) = a$ with $a > 1$ and integrate equation (31) straightforwardly. This way the temperature – and therefore the energy – is specified for the entire domain.

We determine the density at the top and eliminate the pressure P in the equation of hydrostatic equilibrium. Simple integration yields the density for the entire domain. The pressure P is obtained from the equation of state (22).

To complete our model we need to specify the viscosity coefficient η and the radiative conductivity κ . This is achieved by prescribing the Rayleigh number Ra and the Prandtl number $Pr = c_P \eta / K$. The former quantities arise in the definition of the starting model only, since in our model we assume $K(x, t)$ and $\eta(x, t)$ to be constant. This setup simplifies studies of the basic physics while it is still useful for insight into the astrophysically relevant case.

To start dynamics away from equilibrium we apply a random initial perturbation.

3.1.1 *Starting model for the semiconvection problem*

Double-diffusive convection is a phenomenon encountered in chemically inhomogeneous flows where a significant mean molecular weight gradient is present.

Semiconvection is the most important special case of double-diffusive convection in astrophysics. Models of stellar structure and evolution predict settings where the heavier product of nuclear fusion provides stability to a zone which otherwise would be unstable to convective overturning, because temperature sufficiently rapidly decreases against the direction of gravity. Such a zone would become convective, if its composition were mixed, and the question whether such a zone should be treated as if it were mixed or not has become known as the *semiconvection problem* [28].

To model a chemically inhomogeneous fluid we need to add an equation describing the dynamics of the second species to our set of equations. The corresponding partial density equation has been introduced in Section 2. The starting model for a semiconvective simulation has been developed by F. Zaussinger [27] and is set on top of the starting model for stellar convection by expanding it with the specification of the Lewis Number $Le = c_P \rho \kappa_c / K$, which relates the radiative conductivity K to the diffusion coefficient κ_c as well as with the stability parameter R_ρ . The stability parameter is defined as the ratio of the mean molecular weight gradient to the superadiabatic gradient. Further details are found in [27].

3.2 Simulation Setting

Due to the compressible nature of the flows we model, we specify the vertical extent of the simulation domain in multiples of the pressure scale height $H_P = P/(\rho g)$. For the simulations presented the domain always covers 1 H_P .

To determine the resolution required to resolve even the smallest structures in our simulations – namely, to perform a *direct numerical simulation* – we resort to mixing length theory. In [27], a correlation between the Rayleigh number and the diffusion coefficients is derived and a balance between advection by the interior flow and the diffusion across an interface is used to estimate the boundary layer thickness δ_T as

$$\delta_T = Ra_*^{-\frac{1}{4}} H \quad (32)$$

where H denotes the (physical) height of the domain and $Ra_* = Ra \cdot Pr$ is the modified Rayleigh number. If H denotes the number of grid points, then δ_T is the number of grid points resolving the thermal boundary layer.

Similarly, in case of double-diffusive convection, the boundary layer thickness of the second species δ_c follows from the definition of the Lewis Number and scales with the thermal boundary layer thickness,

$$\delta_c = \sqrt{Le} \delta_T \quad (33)$$

The same conclusion can be drawn for the viscous boundary layer,

$$\delta_{\text{visc}} = \sqrt{Pr} \delta_T \quad (34)$$

using here the definition of the Prandtl number Pr .

In our simulations we seek to resolve the boundary layers with a minimum of 5 grid points.

The system of equations is discretized on a rectangular, equidistantly spaced grid. Boundary conditions are based on the assumption that all quantities are periodic in the horizontal direction. Moreover, for the hydrodynamical equations, we employ “closed” (Dirichlet) boundary conditions.

Simulation time is measured in units of *sound crossing times* (*scrt*). One sound

crossing time is defined as the time taking an acoustic wave to propagate from the bottom to the top of the simulation box.

3.3 Numerical Results Part 1

After ascertaining the basic properties of the numerical method as outlined in [12], we turned to simulations of stellar convection and stellar semiconvection. Although for some parameter sets the method performed well and exhibited the higher timestep expected from it, for other parameter sets spurious oscillations appeared in the numerical solution.

In Figure 1 we show snapshots of a simulation of double-diffusive convection. The simulation parameters are $Pr = 1.0$, $Le = 1.0$, $R_\rho = 1.1$ and $Ra = 160000$. We have a spatial resolution of 100×100 grid points and choose a CFL Number of $c_{\text{adv}} = c_{\text{diff}} = 0.15$. After a certain time, two-point instabilities appear in the numerical solution, propagate over the entire domain and render the simulation useless.

We therefore strived to enhance the long-term stability of our solver.

4 Enhancing Stability: Dissipative Spatial Discretization

In the ANTARES framework, the second-order terms have been evaluated via a finite difference scheme of fourth order [10],

$$\begin{aligned} (U_i^n)_{xx} = & \frac{-U_{i+4}^n - 18U_{i+3}^n + 80U_{i+2}^n + 18U_{i+1}^n - 162U_i^n + 18U_{i-1}^n + 80U_{i-2}^n - 18U_{i-3}^n + U_{i-4}^n}{192h^2} \\ & + O(h^4) \end{aligned}$$

This stencil satisfies the properties of flux conservation, easy generalization to more spatial dimensions through directional splitting and easy implementation into conservative numerical schemes for the hyperbolic part of the hydrodynamical equations. However, the following analysis shows that this stencil lacks a crucial property: strict dissipativity.

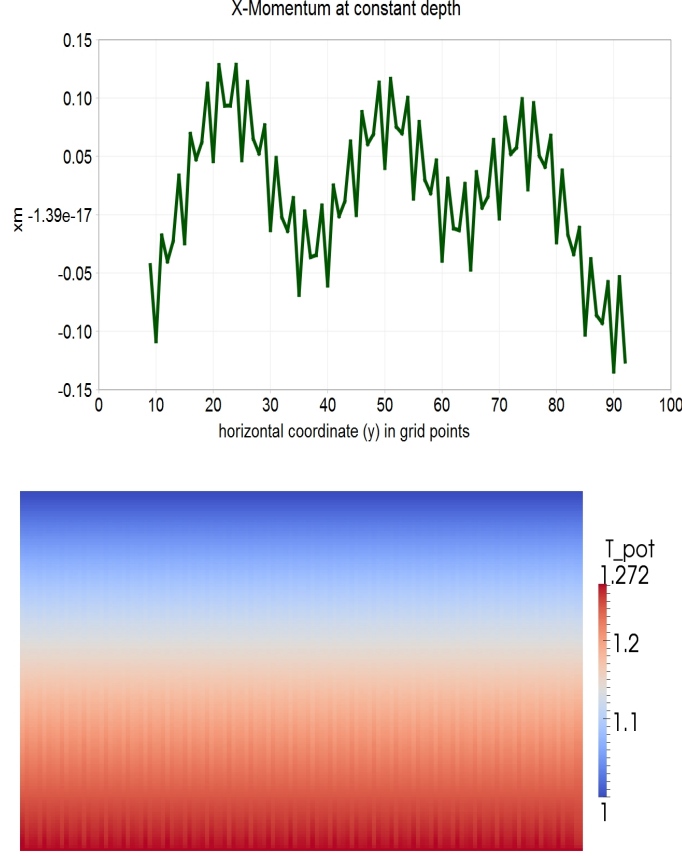


Fig. 1. Simulation of double-diffusive convection. The upper picture shows a horizontal slice of the momentum in x-direction after 47 scrt. Already, two-point instabilities have appeared. 14 scrt later they are ubiquitous and affect every model variable used. This is demonstrated in the lower picture of the potential temperature at 61 scrt.

4.1 Dissipativity Analysis

A dissipative finite difference scheme efficiently damps high-frequency oscillations in the numerical solution. To determine whether our scheme is dissipative or not, we resort to dissipativity analysis (see [23] for the general idea).

The crucial quantity studied in this context is the *amplification factor* $g = g(\theta)$. The propagation of the numerical solution by one time step corresponds to the multiplication of the Fourier transform of the numerical solution by this factor g . Thus, the magnitude of the amplification factor equals the factor by which the amplitude of each frequency in the solution is increased or decreased during each time step. Hence, the finite difference scheme is strictly dissipative if $|g(\theta)| < 1$ for all $\theta \in [-\pi, \pi]$ and $g(0) = 1$. In general, θ depends on the timestep Δt and, therefore, $g(\theta)$ depends on the Runge-Kutta method used

for time integration.

The detailed analysis is given in [10], so we will limit ourselves to the results. It turns out that for both the second and third order TVD Runge-Kutta methods, $g(\theta) = 1$ for $\theta \in \{-\pi, 0, \pi\}$. Thus, both schemes reduce the magnitude of most frequencies (given an accordingly chosen timestep) but not the highest frequencies appearing on the grid scale. This is essentially the property we lack in our simulations.

Therefore, we here derive a finite difference scheme which is dissipative, of fourth order and consistent with the ENO spatial discretization employed for the advective terms of the Navier-Stokes equations.

4.2 Derivation from the WENO approach

We repeat the derivation suggested in [10].

In the WENO-approach [21] the U_i are assumed to be cell averages of a function $v(x)$,

$$U_i = \frac{1}{h} \int_{x_{i-\frac{1}{2}}}^{x_{i+\frac{1}{2}}} v(\zeta) d\zeta \quad (35)$$

Approximating $v(x)$ with a polynomial function $p(x)$ to specified order, $p(x) = v(x) + O(h^5)$, one obtains

$$(U_i)_x = \frac{1}{h} (p(x_{i+\frac{1}{2}}) - p(x_{i-\frac{1}{2}})) + O(h^5) \quad (36)$$

as long as the functions are smooth enough to give an extra h in the difference to cancel that one in the denominator. Clearly, using $p(x_{i+1/2})$ as approximation to $U_{i+1/2}$ has a lower order of accuracy, the higher order comes from perfect cancellation when building the difference. Now using $p'(x \pm 1/2)$ for building the 2nd derivative one obtains

$$(U_i)_{xx} = \frac{p'(x_{i+\frac{1}{2}}) - p'(x_{i-\frac{1}{2}})}{h}. \quad (37)$$

Centered 4-point stencil approximation leads to

$$p_{i+\frac{1}{2}} = \frac{U_{i-1} - 15 U_i + 15 U_{i+1} - U_{i+2}}{12 h} + O(h^2), \quad (38)$$

and

$$p_{i-\frac{1}{2}} = \frac{U_{i-2} - 15 U_{i-1} + 15 U_i - U_{i+1}}{12 h} + O(h^2), \quad (39)$$

where the order of accuracy is measured with respect to $(U_{i\pm 1/2})_x$. The calculation was done using a Mathematica 4.1 script. The second derivative is then given by

$$(U_i^n)_{xx} = \frac{-U_{i-2} + 16U_{i-1} - 30U_i + 16U_{i+1} - U_{i+2}}{12h^2} + O(h^4) \quad (40)$$

which corresponds to the standard centered 5-point stencil approximation.

The corresponding dissipativity analysis in [10] shows that this spatial discretization is dissipative in combination with both Runge-Kutta methods mentioned in Section 2.4. However, this property comes at the cost of an additional restriction to the stability constraint. Monotonic decay of the numerical solution is ensured, if the diffusive Courant Number in (2.4) satisfies

$$c_{\text{diff } 2 \text{ max}} = \frac{3}{4} c_{\text{diff max}} \quad (41)$$

The reader will notice that the dissipativity analysis has been performed assuming (40) to be a finite difference scheme, whereas (40) was derived in a finite-volume framework (e.g. equation (35)). The justification for mixing both approaches is given by Shu in [22]. He shows that for one-dimensional conservation laws the finite-volume and the finite-difference WENO reconstruction procedure is essentially the same. The only difference is found in the input-output pair: for a finite volume scheme, the input is the set of cell averages and the output is the set reconstructed values of the solution at the cell interfaces; for a finite-difference scheme, the input is the set of point values of the physical flux and the output is the numerical fluxes at the cell interfaces. The transition to several dimensions is obtained by dimensional splitting as common in finite difference methods.

5 Numerical Results Part 2

We rerun the simulation of double-diffusive convection shown in Figure 2 employing the dissipative finite difference scheme derived in the previous section. Although the new stencil entails a more severe timestep restriction, we choose the Courant number such that in both simulations the same timestep is used. We see that due to the dissipative property our improved solver efficiently damps the high frequency oscillations on the grid scale and leads to a smooth and stable solution.

It was surprising to find the origin of the mentioned instabilities in the non-

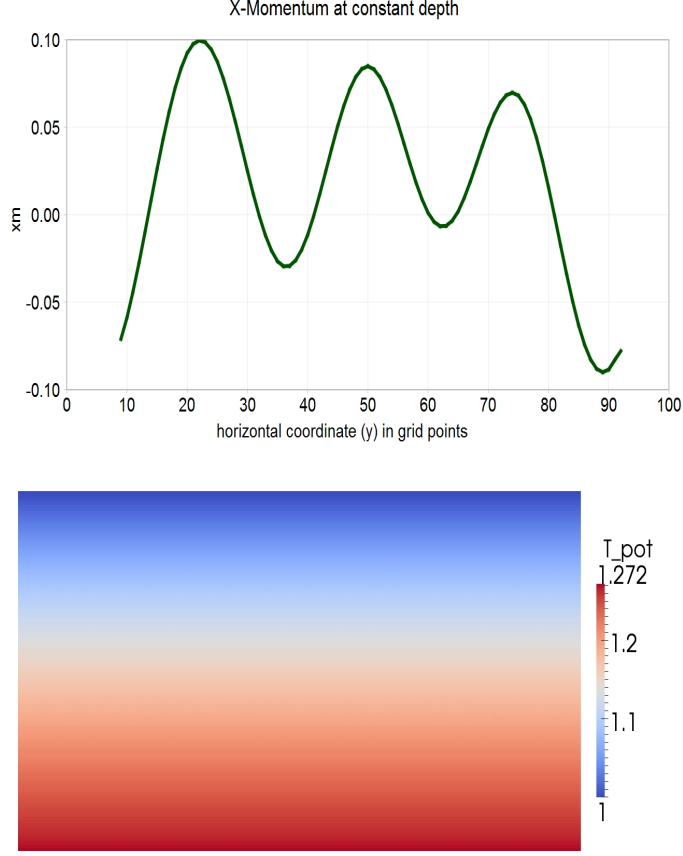


Fig. 2. Rerun of the simulation described in Section 3.3 with strictly dissipative spatial discretization. The upper picture shows a horizontal slice of x-momentum after 47 scrt and the lower picture the potential temperature after 61 scrt. There is no indication of spurious oscillations.

dissipative spatial discretization scheme, since the fully explicit solver which consists of WENO-scheme for evaluation of the hyperbolic part of the NSE and the non-dissipative finite difference scheme (35) did not exhibit similar features for the simulation mentioned in Section 3.3. However, the fully explicit solver is limited by the timestep induced by the sound speed, which is significantly smaller than the timestep permitted by the method of [12]. Furthermore, we also note that some amount of numerical dissipation on the grid scale is provided by the WENO scheme. One property of the Poisson-like equation is that information is propagated infinitely fast, such that any instability appearing in the pressure evolution equation travels instantaneously through the entire domain. Both facts, the large timesteps and the error propagation through (25) may contribute to the fast propagation and build-up of the instabilities appearing on the grid scale.

Having successfully enhanced the longterm stability of the method, we per-

formed a series of simulations of stellar convection and double-diffusive convection. Such a simulation is expected to evolve the following way: after the initial vertical oscillations are damped out³, the velocity field slowly starts building up. Large scale gravity waves form and break, causing the fluid to mix locally. The turbulent mixing process spreads over the whole domain and after a while, quasi-stationary convective rolls form.

In case of the double-diffusive convection scenario, the main difference to the chemically homogeneous convective scenario is that the stable mean molecular weight gradient delays the build-up of the velocity field, leading to a considerable prolongation of the diffusive phase. By the term “diffusive phase” we refer to the first part of the simulation, where the fastest timescale is set by diffusion processes. Eventually, the fluid velocity increases such as to pose an even greater restriction on the timestep than diffusion. Once this happens, the simulation has reached the “advective phase”.

Figure 3 shows the timestep evolution in a simulation of stellar convection. The maximum timestep advantage compared to the explicit scheme is achieved in the diffusive phase of the simulation, which lasts in this case approximately 30 scrt. The build-up of the velocity field is best followed by looking at the mean Mach number. In the range of 10-20 scrt the velocity steadily increases, until the first gravity waves break at approximately 22 scrt. The mixing process slows the growth of the velocity until it reaches a steady state of convective motions (at approximately 55 scrt). At a certain point, the fluid velocity is high enough to pose a greater restriction on the timestep. Nevertheless, even in the final state with quasi-stationary averaged properties the timestep employed is still twice the sound-speed based timestep.

Figure 4 depicts the timestep evolution in a simulation of semiconvection. Here we encounter a real low Mach number regime since the Mach number never exceeds 0.2 and we see that the relevant timestep restriction stems from diffusive processes which leads to a timestep nearly 5 times higher than τ_{snd} .

5.1 Further Tests

To gain insight into the capabilities and limits of the method, we also ran some standard test cases which are usually set up for the Euler equations.

³ These oscillations arise because due to rounding errors and due to the different truncation errors of the integration of the initial condition and the spatial discretization of the dynamical equations in the setup of the starting model the simulation is not in perfect hydrostatic equilibrium.

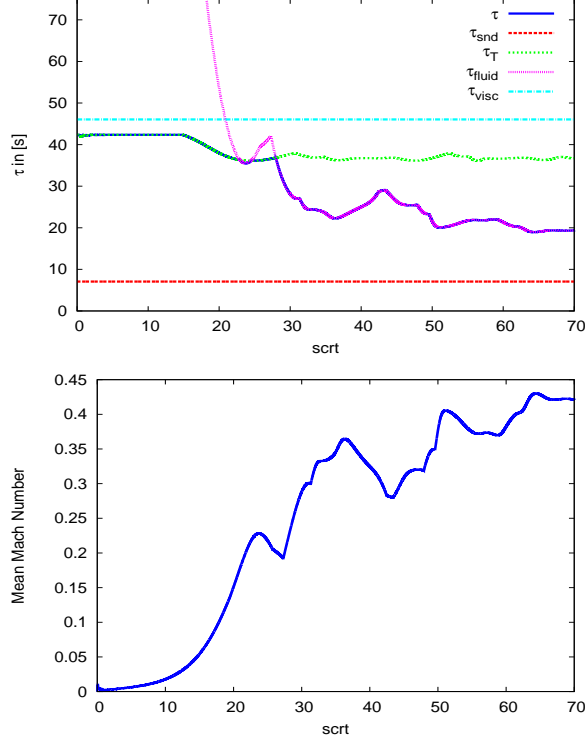


Fig. 3. Simulation of stellar convection with parameters $Pr = 1.0$ and $Ra = 160000$. The spatial resolution is 150×150 grid points and we use a Courant number $c_{adv} = c_{diff} = 0.2$. Simulation time is 70 $sctr$.

Note that in these tests the original method of [12] is used.

Firstly, we have rerun the Sod shock tube test presented in [12] and report to have obtained similar results. This indicates that the solver is capable of handling shock waves correctly and therefore its applicability is not limited to the low Mach number regime. We also reproduced the sound-speed based Courant number of 300 in the smooth flow test.

However, many compressible flow solvers require special techniques to compute an accurate numerical solution of the governing equations in the incompressible limit (see [6,7,24]). To determine the behaviour of this method in such a setting we resort to the Gresho vortex problem.

5.1.1 The Gresho Vortex Problem

The Gresho vortex is a time-independent rotation pattern. Angular velocity depends only on the radius and centrifugal force is balanced by the pressure gradient. The original setup is found in [14]. We use the slightly modified initial condition of [15], which permits the variation of the Mach number.

We use a cartesian domain $[0,1] \times [0,1]$ and employ periodic boundary

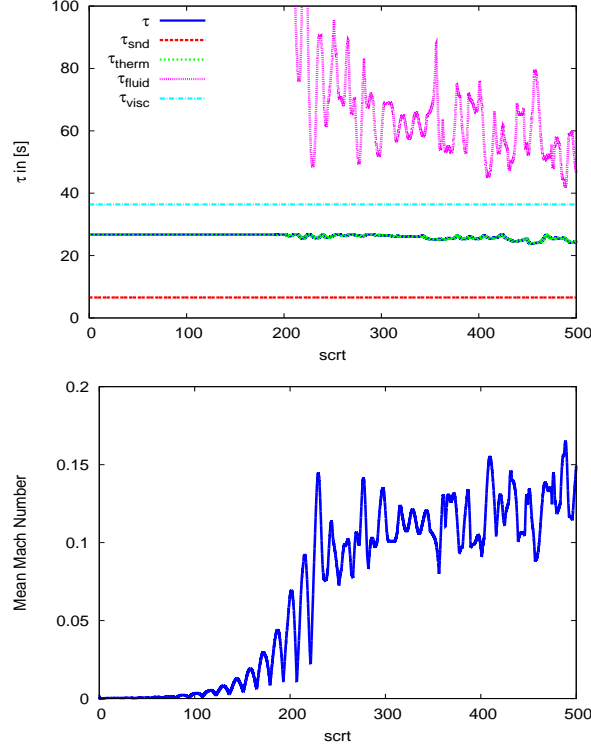


Fig. 4. Simulation of double-diffusive convection with parameters $Pr = 1.0$, $Ra = 160000$, $Le = 0.5$ and $R_\rho = 1.1$. The spatial resolution is 150×150 grid points and we use a Courant number $c_{\text{adv}} = c_{\text{diff}} = 0.2$.

conditions. The initial condition is given dependent on the radius $r = \sqrt{(x - 0.5)^2 + (y - 0.5)^2}$ as

$$\rho = 1.0 \quad (42)$$

$$P_0 = \frac{\rho}{\gamma Ma^2} \quad (43)$$

$$u_\phi = \begin{cases} 5r & \text{if } 0 \leq r \leq 0.2 \\ 2 - 5r & \text{if } 0.2 \leq r \leq 0.4 \\ 0 & \text{if } 0.4 \leq r \end{cases} \quad (44)$$

$$P = \begin{cases} P_0 + \frac{25}{2}r^2 & \text{if } 0 \leq r \leq 0.2 \\ P_0 + \frac{25}{2}r^2 + 4(1 - 5r - \ln(0.2) + \ln(r)) & \text{if } 0.2 \leq r \leq 0.4 \\ P_0 - 2 + 4\ln(2) & \text{if } 0.4 \leq r \end{cases} \quad (45)$$

Ma denotes the Mach number and u_ϕ denotes the angular velocity. The cartesian velocity components are obtained via

$$u_x = -\sin(\theta) u_\phi \quad (46)$$

$$u_y = \cos(\theta) u_\phi \quad (47)$$

where $\theta = \text{atan2}(y - 0.5, x - 0.5)$.

We run the Gresho vortex test with $\text{Ma}=0.1$, $\text{Ma}=0.01$ and $\text{Ma}=0.001$. Figure 5 compares the results obtained in this setting by the semi-implicit method and the fully explicit solver. In this test, both solvers use , for proper comparison, the same sound-speed induced timestep and a Courant number of 0.5. The simulation time is 2 sec.

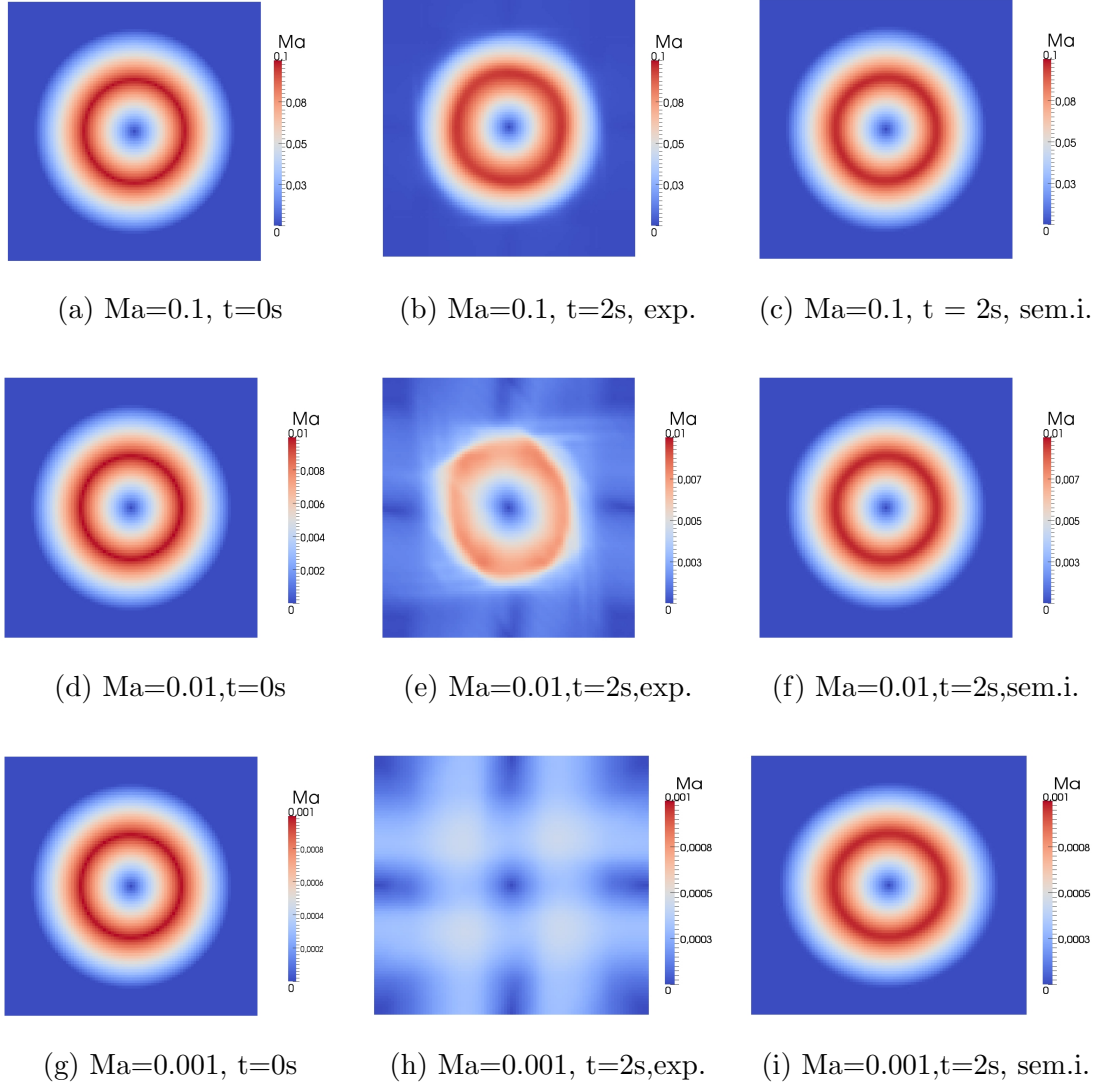


Fig. 5. Comparison of the Gresho vortex test performed with the explicit and the semi-implicit solver with different Mach numbers. On the left, the initial configuration is depicted. In the center and on the right, the simulation is advanced 2 sec with the explicit solver and the semi-implicit solver, respectively.

The results show that for $\text{Ma}=0.1$ both solvers yield similar results, although the dissipation of kinetic energy is higher in the explicit solver (see also Figure 6). However, as the Mach number drops, the dissipation of the explicit solver

increases and leads to inaccurate results. The dissipation of the solver of [12] on the other hand seems to be independent of the Mach number.

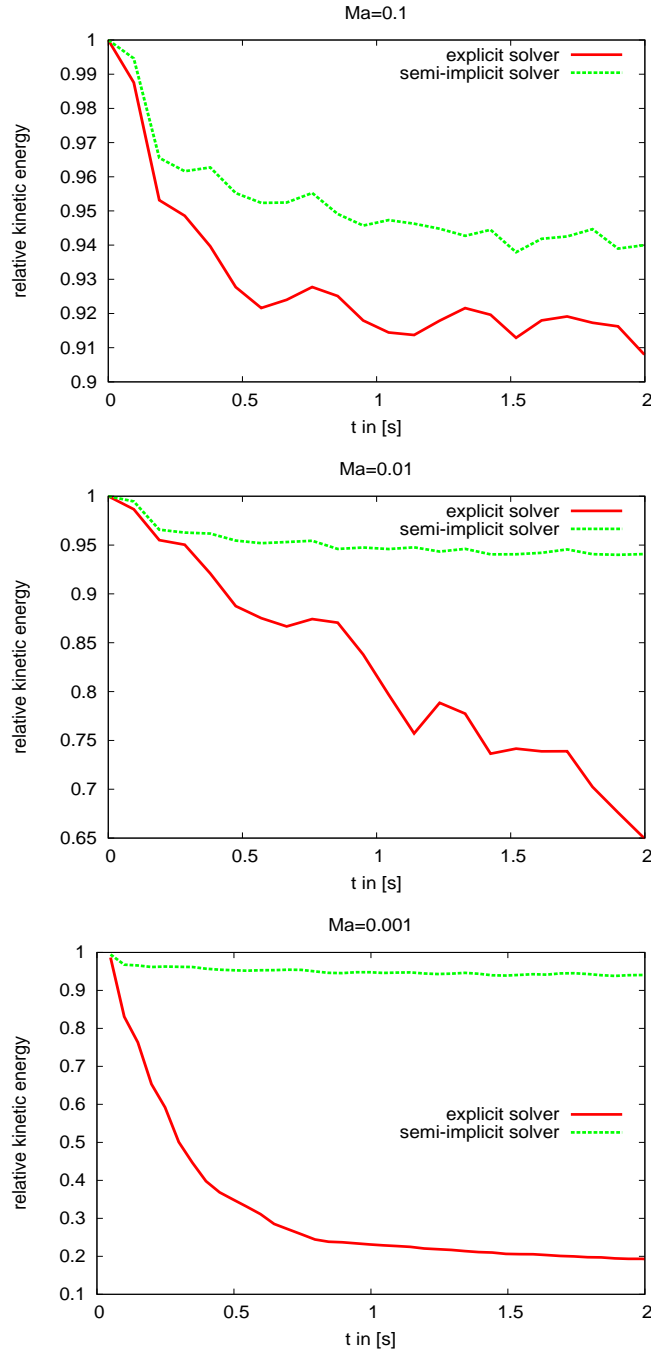


Fig. 6. We compare the relative kinetic energy predicted by the simulations over time. Whereas the dissipation of the explicit solver increases dramatically as the Mach number drops, the dissipation of the semi-implicit method is independent of the Mach number for exactly the same number of timesteps.

Since the semi-implicit method theoretically allows the simulation to be advanced with a timestep higher than the one induced by the sound speed, we

have rerun the Gresho vortex test with $Ma=0.001$ and the semi-implicit solver, advancing it by multiples of the sound-speed induced timestep. We find that the simulation remains stable for up to four times the explicit timestep. Figure 7 shows no adverse effects on the dissipation from choosing a larger timestep.

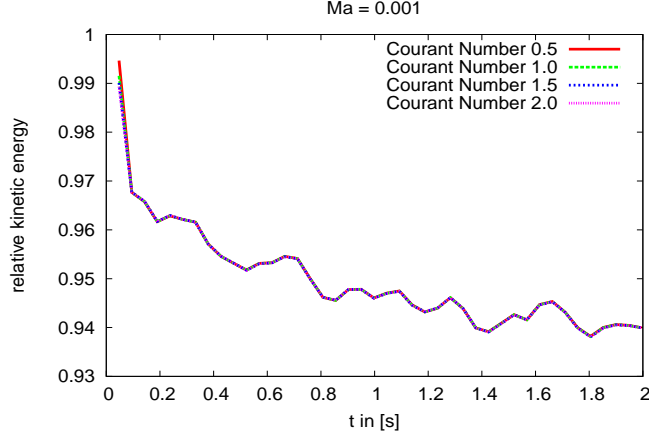


Fig. 7. Courant number tests with the semi-implicit method. Advancing the Gresho vortex with $Ma=0.001$ with a greater timestep does not affect the dissipation of the scheme.

6 Conclusions and Outlook

We have tested the numerical method of [12] in the low Mach number limit as well as its performance in high Mach number flows. Apart from approaching correctly the incompressible limit of the compressible equations for fluid flow, it allows simulations to be advanced with a timestep significantly higher than a fully explicit solver and contrarily to most solver designed for simulations of that kind, it is capable of passing smoothly to regimes with higher fluid velocities and even handles shock waves correctly. Thus it is applicable to a wide range of problems.

Furthermore, we have generalized this approach to the more complex Navier-Stokes equations and successfully enhanced the stability of the overall scheme, making it thus suitable to more realistic long-term simulations of astrophysical processes.

However, in some settings within our parameter range, the timestep restriction due to diffusive processes is also severe and in some cases it is even more restrictive than the acoustic timestep restriction (see Figure 8). Note that the resolution is somewhat lower in this case (only 3 grid points resolve the diffusive boundary layer), but for the present purpose this is sufficient, especially since at high resolution the diffusive timescales are even more restrictive.

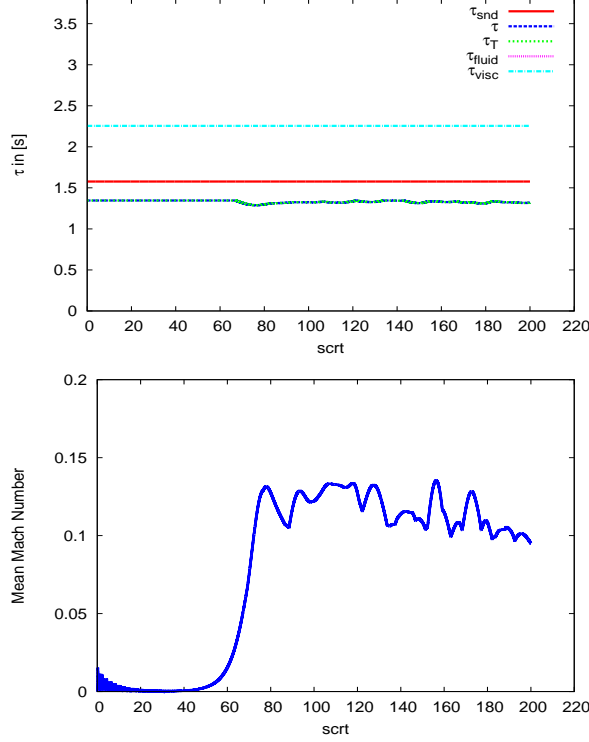


Fig. 8. Simulation of double-diffusive convection with parameters $Pr = 1.0$, $Ra = 160000$, $Le = 0.01$ and $R_\rho = 1.3$. The spatial resolution is 600×400 grid points. Note that in this setting diffusion poses an even greater restriction on the timestep than sound waves.

Following the idea of integrating terms describing processes acting on short timescales implicitly, we have combined total-variation diminishing implicit-explicit (TVD IMEX) Runge-Kutta methods with our solver. This combination treats the diffusive terms implicitly and therefore alleviates the timestep restrictions due to diffusive processes. In [11] TVD IMEX Runge-Kutta methods are analysed in detail and the fruitful junction of our solver and those methods is demonstrated.

References

- [1] A. Arakawa, C. S. Konor, Unification of the anelastic and quasi-hydrostatic systems of equations, *Monthly Weather Review* 137 (2009) 710–726.
- [2] R. Fedkiw, B. Merriman, S. Osher, Efficient characteristic projection in upwind difference schemes for hyperbolic systems, *Journal of Computational Physics* 141 (1998) 22–36.
- [3] R. P. Fedkiw, X.-D. Liu, S. Osher, A general technique for eliminating spurious oscillations in conservative schemes for multiphase and multispecies Euler

- equations, *Int. Journal of Nonlinear Sciences and Numerical Simulations* 3 (2002) 99–106.
- [4] S. Gottlieb, C.-W. Shu, Total variation diminishing Runge-Kutta schemes, *Mathematics of Computation* 67 (221) (1998) 73–85.
 - [5] H. Grimm-Strele, Numerical solution of the generalised poisson equation on parallel computers, Master’s thesis, Universität Wien, available from http://othes.univie.ac.at/9200/1/2010-03-18_0404659.pdf (März 2010).
 - [6] H. Guillard, On the behavior of upwind schemes in the low Mach number limit. 4.: P0 approximation on triangular and tetrahedral cells, Tech. Rep. 6898, Centre de recherche INRIA Sophia Antipolis, Institut National de recherche en informatique et en automatique, <http://hal.inria.fr/docs/00/37/49/25/PDF/RR-6898.pdf> (2009).
 - [7] H. Guillard, A. Murrone, On the behavior of upwind schemes in the low Mach number limit: 2. Godunov type schemes, *Computers and Fluids* 33 (2004) 655–675.
 - [8] W. Hillebrandt, F. Kupka, Interdisciplinary aspects of turbulence, in: *Lecture Notes in Physics: An Introduction to Turbulence*, vol. 756, Springer-Verlag Berlin Heidelberg, 2009, pp. 1–20.
 - [9] G.-S. Jiang, C.-W. Shu, Efficient implementation of weighted ENO schemes, *Journal of Computational Physics* 126 (1996) 202–228.
 - [10] O. Koch, F. Kupka, B. Löw-Baselli, A. Mayrhofer, F. Zaussinger, SDIRK methods for the ANTARES code, ASC Report 32/2010, Inst. for Anal. and Sci. Comput., Vienna Univ. of Technology, available from <http://www.asc.tuwien.ac.at/preprint/2010/asc32x2010.pdf> (2010).
 - [11] F. Kupka, N. Happenhofer, I. Higuera, O. Koch, Total-variation-diminishing implicit-explicit Runge-Kutta methods for the simulation of double-diffusive convection in astrophysics, submitted to *J. Comput. Phys.* (2011) (preprint available at <http://arxiv.org/abs/1106.5672>) (2011).
 - [12] N. Kwatra, J. Su, J. T. Grétarsson, R. Fedkiw, A method for avoiding the acoustic time step restriction in compressible flow, *Journal of Computational Physics* 228 (2009) 4146–4161.
 - [13] L. Landau, E. Lifshitz, *Fluid Mechanics*, Pergamon Press, 1963.
 - [14] R. Liska, B. Wendroff, Comparison of several difference schemes on 1D and 2D test problems for the Euler equations, *SIAM Journal of Scientific Computing* 25 (2003) 995–1017.
 - [15] F. Miczek, Low mach number hydrodynamics, personal communication (2011).
 - [16] D. Mihalas, B. Mihalas, *Foundations of radiation hydrodynamics*, Oxford University Press, 2004.

- [17] M. Motamed, C. Macdonald, S. Ruuth, On the linear stability of the fifth-order WENO discretization, *Journal of Scientific Computing* 47 (2011) 125–149.
- [18] H. Muthsam, W. Göb, F. Kupka, W. Liebich, Interacting convection zones, *New Astronomy* 4 (1999) 405–417.
- [19] H. Muthsam, F. Kupka, B. Löw-Baselli, C. Obertscheider, M. Langer, P. Lenz, ANTARES - A Numerical Tool for Astrophysical RESearch with applications to solar granulation, *New Astronomy* 15 (2010) 7460–475.
- [20] Y. Ogura, N. A. Phillips, Scale analysis of deep and shallow convection in the atmosphere., *Journal of Atmospheric Sciences* 19 (1962) 173–179.
- [21] C.-W. Shu, Essentially non-oscillatory and weighted essentially non-oscillatory schemes for hyperbolic conservation laws, ICASE Report No. 97-65.
- [22] C.-W. Shu, High order weighted essentially non-oscillatory schemes for convection dominated problems, *SIAM Review* 51 (2009) 82–126.
- [23] J. C. Strikwerda, *Finite Difference Schemes and Partial Differential Equations*, Wadsworth & Brooks /Cole Advanced Books & software, 1989.
- [24] B. Thornber, A. Mosedale, D. Drikakis, D. Youngs, R. Williams, An improved reconstruction method for compressible flows with low Mach number features, *Journal of Computational Physics* 227 (2008) 4873–4894.
- [25] R. Wang, R. Spiteri, Linear instability of the fifth-order WENO method, *SIAM Journal of Numerical Analysis* 45 (2007) 1871–1901.
- [26] A. Weiss, W. Hillebrandt, H.-C. Thomas, H. Ritter, Cox & Giuli’s *Principles of Stellar Structure*, extended second ed., Cambridge Scientific Publishers Ltd, 2004.
- [27] F. Zaussinger, Numerical simulation of double-diffusive convection, Ph.D. thesis, University of Vienna, available from <http://othes.univie.ac.at/13172/> (December 2010).
- [28] F. Zaussinger, H. Spruit, Semiconvection, submitted to *Astronomy and Astrophysics* (preprint available at <http://arxiv.org/abs/1012.5851>) (2011).